ACS APPLIED MATERIALS & INTERFACES

www.acsami.org Research Article

Phase-Selective Growth of Ferroelectric and Antiferroelectric $NaNbO_3$ Thin Films

Baichen Lin, Qibin Zeng, Ping Yang, Shengwei Zeng, Zhi Shiuh Lim, Tiancheng Luo, Weifan Cai, Samantha Faye Duran Solco, Zhen Ye, Celine Sim, Jinlong Xu, Mengyao Xiao, Khuong Phuong Ong, Chee Kiang Ivan Tan, Seeram Ramakrishna, Mark B. H. Breese, Chengkuo Lee, Kaiyang Zeng, Yeng Ming Lam,* and Huajun Liu*

Cite This: https://doi.org/10.1021/acsami.5c21649 Read Online

ACCESS | Metrics & More | Article Recommendations | Supporting Information

ABSTRACT: Ferroelectric and antiferroelectric materials play a critical role in electrical, optical, and thermal devices due to their electric field-controlled polarization switching capability. Controlling phase formation during thin film growth is essential for the design of these devices. In this study, we separately stabilized pure ferroelectric rhombohedral (N phase) and pure antiferroelectric orthorhombic (P phase) structures by precisely controlling the growth conditions of 70 nm-thick $NaNbO_3$ (NNO) thin films on (111)-oriented Nb-doped $SrTiO_3$ substrates. Through reciprocal space mappings and quarter-order diffraction measurements, a twinning structure within the NNO P-phase film is resolved. An antiferroelectric-to-ferroelectric phase transition, accompanied by a substantial enhancement in the electromechanical coupling response, is observed in the NNO P-phase film. Importantly, a phase diagram is constructed to delineate the growth window for each phase. This work provides a framework for synthesizing NNO thin films with controlled phases and offers a strategy for designing functional ferroelectric and antiferroelectric devices.

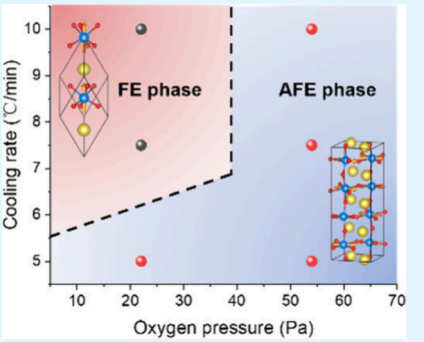

KEYWORDS: *$NaNbO_3$, thin films, ferroelectric, antiferroelectric, phase diagram*

INTRODUCTION

Polarization switchable materials, like ferroelectric (FE) and antiferroelectric (AFE) materials, have been extensively investigated due to their promising applications in electronic transistor devices,[1,2] switching devices,[3] microelectromechanical systems (MEMS),[4,5] and energy storage.[2,6] Among them, lead-free perovskite oxide, $NaNbO_3$ (NNO), has recently attracted an increasing amount of attention due to its environmentally friendly nature and outstanding electromechanical coupling properties.[7,8] NNO goes through a paraelectric (PE) (space group $Pm3m$) → PE ($P4/mbm$) → PE ($Ccmm$) → PE ($Pnmm$) → AFE ($Pmnm$) → AFE ($Pbcm$) → FE ($R3c$) phase transition from high to low temperatures.[9] Bulk NNO has a rhombohedral phase (N phase, $R3c$) when the temperature is below −100 °C and a lattice constant of a_c = 3.90(8) Å and α_c = 89.2(2)° (the subscript c represents the pseudocubic notification) at −150 °C (Figure 1a, top panel).[10,11] In N-phase NNO, the switchable spontaneous polarization along (111) is indicative of its FE properties. With an increase in temperature, bulk NNO will undergo a first-order phase transition and change to orthorhombic phase (P phase, $Pbcm$) with lattice parameters a_o = 5.50(1) Å, b_o = 5.56(2) Å, and c_o = 15.53(7) Å (the subscript o represents the orthorhombic notification) at room temperature (Figure 1a, bottom panel).[12] Different from N-phase NNO, the P phase has an antipolar structure,[13] showing AFE properties. Interestingly, the NNO P phase usually shows an irreversible ferroelectric polarization loop rather than a double polarization loop at room temperature due to the small energy difference between the AFE P and FE Q (space group, $Pmc2_1$) phases.[14,15] The field-induced orthorhombic FE phase is a metastable state, which might change back to the AFE P phase after application of a short electric pulse of opposite polarity.[16] Furthermore, NNO shows a multiphase competitive ground state as demonstrated in an electric field (E)−temperature (T) phase diagram, which depicts a region in which the P, N, and Q phases coexist.[16] This may be because the NNO FE N phase also has a small energy difference compared to the AFE P phase.[17]

NNO-based bulk single crystals and ceramics have been investigated and applied for more than 50 years.[18] NNO thin

Received: October 28, 2025
Revised: February 8, 2026
Accepted: February 13, 2026

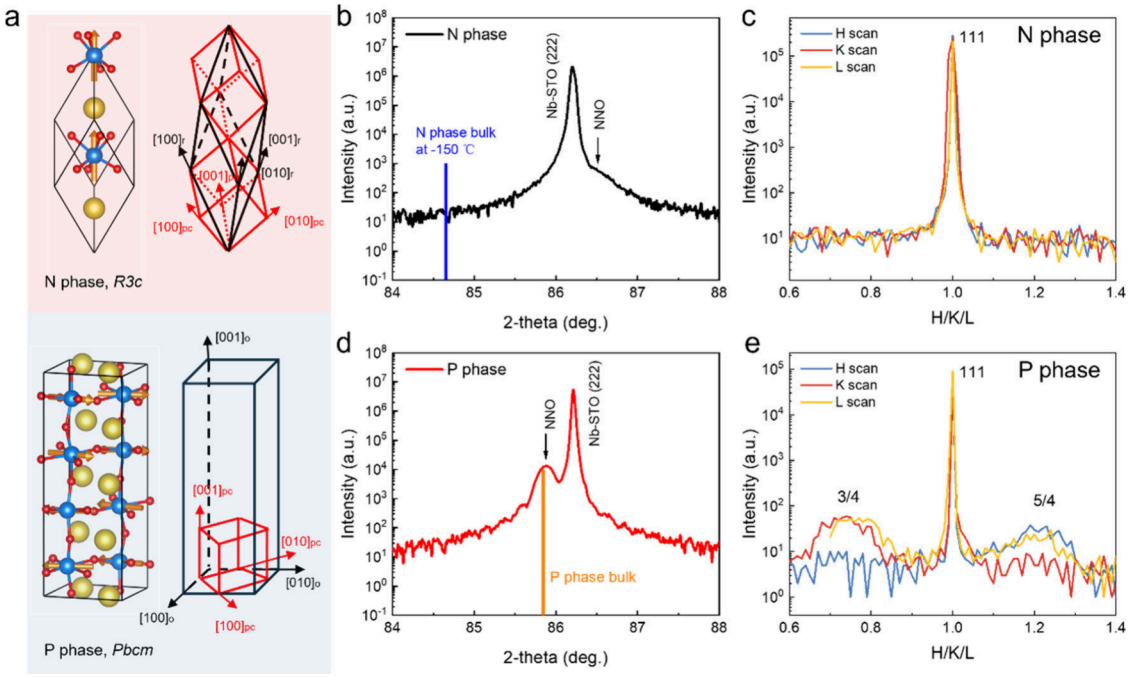

Figure 1. X-ray diffraction (XRD) characterization of the 70 nm-thick N-phase and P-phase NNO films. (a) Schematic crystal structure of the NNO ferroelectric N phase (top panel, space group *R*3*c*) and antiferroelectric P phase (bottom panel, space group *Pbcm*). (b) X-ray diffraction (XRD) patterns of the N-phase NNO film. (c) Synchrotron X-ray H/K/L scans of the N-phase film. (d) X-ray diffraction (XRD) patterns of the P-phase films. (e) Synchrotron X-ray H/K/L scans of the P-phase film. The solid blue and orange lines represent the 2θ degrees of the N-phase and P-phase NNO (222) peaks, calculated using the bulk lattice parameters for the N phase and P phase, respectively.

films are more attractive for microelectronic devices like MEMS and nonvolatile random-access memories.[2,19] To achieve these applications, sol−gel[20] and pulsed laser deposition (PLD)[21] methods were developed to fabricate NNO thin films. However, these films usually show a polycrystalline nature[20] or an impurity phase.[21] This impurity phase is generally regarded as the Na_3NbO_4 phase resulting from a sodium-rich target or growth conditions.[22] Apart from the impurity phase, the Na:Nb ratio also plays an important role in manipulating the structural properties.[7,22] Therefore, fabrication of high-quality NNO films with different phases and modulation of their properties have not yet been fully investigated. In particular, a pure NNO N phase stabilized at room temperature has not yet been reported, to the best of our knowledge.

Strain engineering is one of the most effective methods for controlling the crystal structures and properties of functional thin films. For example, the polarization in NNO thin films switches from the out-of-plane to in-plane direction upon application of epitaxial strain from compressive to tensile, accompanied by a change from antiferroelectric to ferroelectric phase.[23] A change from a single vertical FE domain to mixed multiple domains was observed in ultrathin NNO films with a strain from compressive to tensile.[24] In addition, an anisotropic in-plane strain could give rise to the monoclinic distortion of NNO thin films.[25] Perovskite oxide $SrTiO_3$ (STO) shows small lattice mismatches of approximately 0.08% and −0.05% for the NNO N phase and P phase, respectively, indicating that the lattice distortion energy has an insignificant influence on the total free energy. The fact that the Gibbs free energy of the NNO N phase is slightly higher than that of the P phase[17] suggests that controlling the growth kinetics might be needed to obtain a single NNO N phase. Substrate orientational engineering plays an important role in controlling the crystal orientation, and even the symmetry of the epitaxial perovskite oxide thin films, upon application of strain and induction of oxygen octahedral rotation.[26−29] Such a strategy demonstrated that the crystallographic orientation is the critical determinant of the structural and multiferroic properties of perovskite oxide thin films.[30] For instance, a previous study suggests that the domain structure and dielectric properties of the NNO films are related to their orientation direction.[31] Since the NNO N phase has a rhombohedral structure, (111)-oriented STO substrates were applied here to induce symmetry constraints to stabilize the N phase.

Here, the 70 nm-thick NNO thin films with a distinct ferroelectric rhombohedral N phase and an antiferroelectric orthorhombic P phase were epitaxially grown on a (111)-oriented Nb-doped STO (Nb:STO) substrate by PLD. A twinning structure in the NNO P-phase film was resolved by reciprocal space mapping and quarter-order diffraction measurements. A phase diagram delineating the growth conditions for the N-phase and P-phase NNO films has been established. Specifically, the modified growth conditions include controlling the air pressure and cooling rate during the growth process. An irreversible phase transition from the AFE to FE phase, accompanied by a significant enhancement of the electromechanical coupling response, was observed by combining piezoresponse force microscopy (PFM) and laser Doppler vibrometer (LDV) measurements.

RESULTS AND DISCUSSION

Structure of the N-Phase and P-Phase NNO Films

To understand the crystal structure of these NNO films, high-resolution X-ray diffraction (XRD) measurements were performed. The low-angle X-ray reflectivity (XRR) patterns

https://doi.org/10.1021/acsami.5c21649
ACS Appl. Mater. Interfaces XXXX, XXX, XXX−XXX

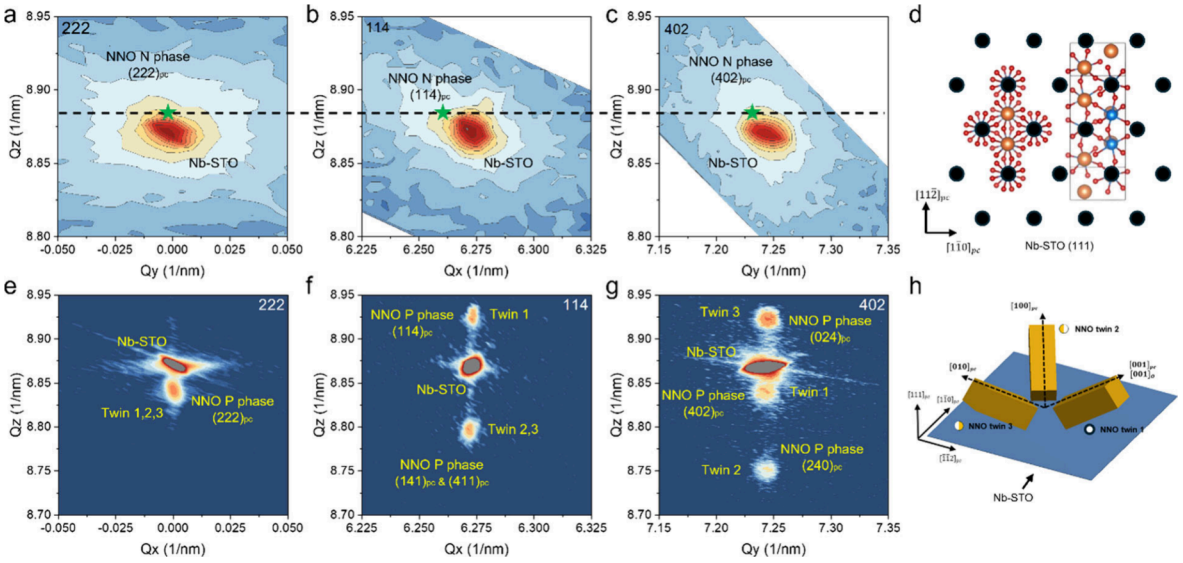

Figure 2. X-ray reciprocal space mapping (RSM) measurements of NNO films. N-phase film: (a) (222), (b) (114), and (c) (402) reflections. The reflection peaks of the NNO N-phase film are marked by green stars. (d) Schematic illustration of the NNO N- and P-phase matching with the (111)-oriented Nb:STO substrate. P-phase film: (e) (222), (f) (114), and (g) (402) reflections. (h) Schematic illustration of domain arrangements in P-phase NNO films.

of the N-phase and P-phase NNO films indicate a thickness of approximately 70 nm; additionally, the well-defined reflectance fringes demonstrate both the high crystalline quality of the NNO films and the good smoothness of their surfaces and interfaces (Figure S1a). Only (111) and (222) diffraction peaks from both the Nb:STO substrate and NNO films are observed in the XRD θ–2θ scans, confirming single-orientation epitaxial growth without impurity phases (Figure S1b). Here, cubic indices are used throughout unless stated otherwise. Figure 1b presents finer XRD θ–2θ scans around the (222) diffraction peak of the N-phase NNO films. The out-of-plane lattice parameter derived from the (222) reflection of the N-phase NNO film is ∼1.125 Å, indicating that the N-phase NNO film exhibits a substantial discrepancy between its film lattice *d*-spacing and bulk value (blue line). Note that the lattice parameters of the pure bulk NNO N phase were measured at −150 °C.[11] Thus, these lattice parameters, including bond length and angle, may change when the NNO N phase is stabilized at room temperature, leading to a significant difference in (222) *d*-spacing. Figure 1c shows the quarter-order diffraction scans of the N-phase NNO film. No quarter-order diffractions were observed, excluding the existence of the AFE structure, which is consistent with the *R*3*c* structure.

In contrast, the out-of-plane lattice parameter (d) derived from the (222) reflection of the P-phase NNO film is 1.131 Å, which is slightly smaller than that of the bulk NNO P-phase $(048)_o$ *d*-spacing value (orange line) (Figure 1d), suggesting a *Pbcm* structure of the P-phase film under a small in-plane tensile strain. The observation of pronounced thickness fringes (Laue oscillations) adjacent to the NNO diffraction peaks signifies coherent lattice ordering, a high degree of crystalline perfection, and an atomically smooth interface. Furthermore, quarter-order diffractions along H/K/L scans reveal the AFE structure and possible twin arrangement in the P-phase NNO film (Figure 1e). This also implies that the slight tensile strain imposed by the substrate constraint may have a negligible effect on the antiferroelectric structure of the P-phase film, while potentially promoting the formation of a preferential twin domain configuration.

To further analyze the crystal structure of the NNO films, reciprocal space mapping (RSMs) measurements were performed. Panels a–c of Figure 2 show the RSMs of the NNO N phase along the (222), (114), and (402) substrate reflections, respectively. The reflection peaks of the corresponding thin film closely overlap with those of the substrate, even using the synchrotron X-ray line scan (Figure S2), making it difficult to precisely determine its lattice constant. However, since the diffraction peaks are well aligned at the same Q_z height (indicated by the black dashed line in Figure 2a–c), it can be inferred that the thin film adopts the rhombohedral *R*3*c* structure among the various phases of NNO, i.e., the N phase. Based on the above, the approximate lattice constants of the N-phase NNO film are a_c = 3.90(4) Å, b_c = 3.90(4) Å, c_c = 3.90(4) Å, and $\alpha_c = \beta_c = \gamma_c = 90.1°$ in pseudocubic notation. Furthermore, the RSM at the (114) reflection reveals that the diffraction peak of the N-phase thin film shows a small shift with that of the substrate in the in-plane direction (Q_x), indicating the presence of lattice strain relaxation in the film. Figure 2d shows that the NNO N phase has a more compatible lattice structure with the Nb:STO (111) substrate compared to that of the NNO P phase. Due to this slight structural mismatch between the NNO P phase and Nb:STO substrate, the P-phase film may tend to form a twin structure to compensate for the interface distortion energy, for instance, the formation of twins in $BiFeO_3$ thin films with monoclinic M_C or M_A phases.[32,33] Here, the P-phase NNO film forms a 3-fold twin structure to minimize the potential structural distortion between the epitaxial film and the substrate. In this case, the P-phase NNO thin film can remain a coherently epitaxially strained thin film without exhibiting lattice relaxation, as evidenced by the same in-plane lattice (Q_x and Q_y) as that of the Nb:STO substrate at nonspecular reflections (Figure 2d–f). These twins with an orthorhombic crystal structure contribute to the splitting of diffraction peaks in the (114) and (402) RSMs. The real indices of all reflections from

https://doi.org/10.1021/acsami.5c21649
ACS Appl. Mater. Interfaces XXXX, XXX, XXX−XXX

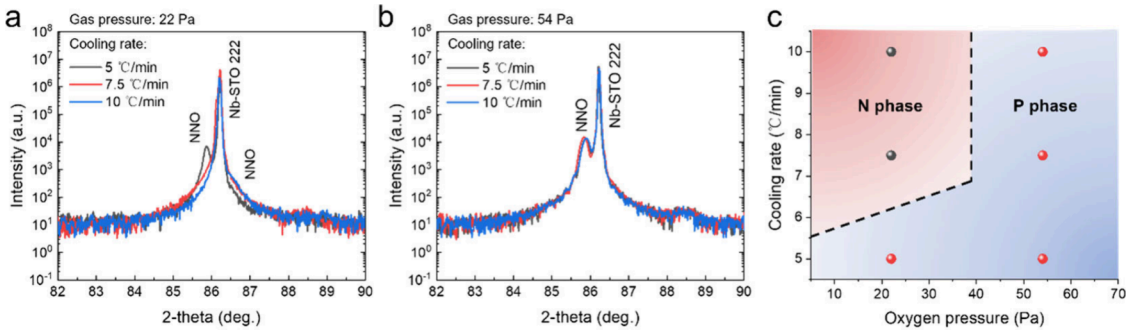

Figure 3. XRD patterns of the NNO films grown at oxygen partial pressures of (a) 22 and (b) 54 Pa with varying cooling rates. (c) Phase diagram of the 70 nm-thick NNO films.

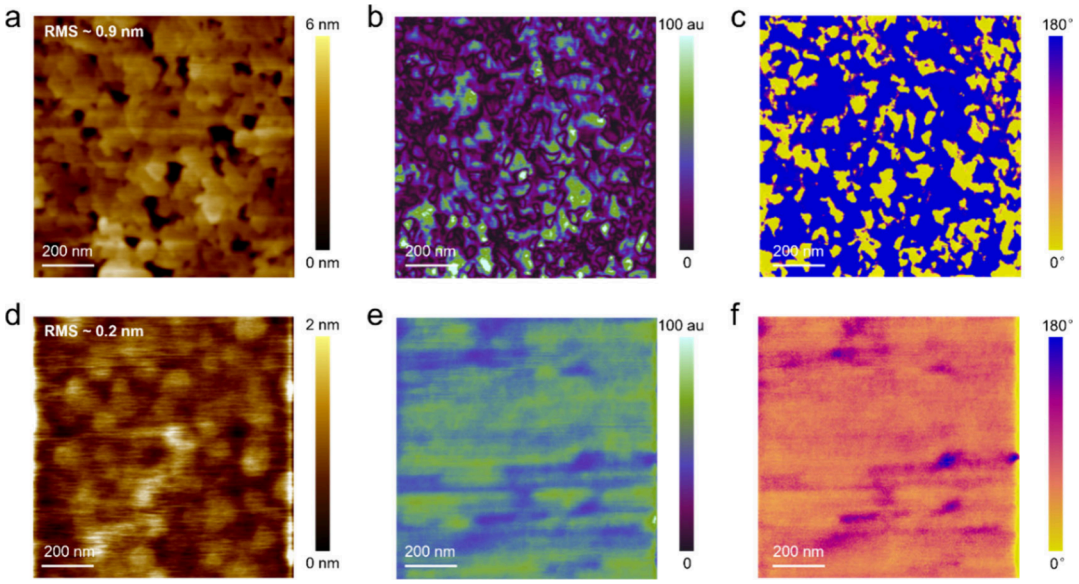

Figure 4. PFM measurements of the NNO films: (a) topography, (b) PFM amplitude, and (c) PFM-phase image of the N-phase NNO film and (d) topography, (e) PFM amplitude, and (f) PFM-phase image of the P-phase NNO film. AC drive of 0.8 V_{pp}.

different twins are given in the corresponding RSMs. Using these indices, the pseudocubic lattice parameters of the NNO P-phase film could be calculated by the RSV method[34] and are as follows: a_c = 3.922 Å, b_c = 3.922 Å, c_c = 3.885 Å, α_c = 90°, β_c = 90°, and γ_c = 89.5°. The lattice constants of the NNO bulk N phase, P phase, and 70 nm-thick films are summarized in Table S1. The converted orthorhombic lattice parameters of the NNO P-phase film are as follows: a_o = 5.523 Å, b_o = 5.570 Å, and c_o = 15.540 Å. These are also indicative of a slight tensile strain due to substrate constraint.

To better understand the relationship between the twin structure and the RSM results, a structural model is shown in Figure 2h. Here, it is assumed that three variants of orthogonal twin grains are distributed on a (111)-oriented Nb:STO substrate, exhibiting 3-fold symmetry based on the clamping properties of the (111)-oriented substrate. These variants are distinguished and labeled with the numerals 1−3 using three circles. The $[001]_o$ directions of NNO twins 1−3 align well with the [001], [100], and [010] directions of the substrate lattice, respectively. In this case, the $(048)_o$ planes of all twins are parallel to the (222) plane of the substrate, leading to the single reflection peak of the NNO film in the (222) RSM (Figure S3a). For the (114) RSM, the in-plane direction is along [−1−12] (Q_x), where NNO twin 2 and NNO twin 3 have the same contributions to the reflection but are different from NNO twin 1. This means that the (114) reflection peak splits into two reflections. The upper peak is fully generated by NNO twin 1, and another is contributed by twins 2 and 3 as demonstrated in the schematic (Figure S3b). Similarly, the in-plane direction was changed to [1−10] (Q_y) to perform (402) RSM. The (402) reflection of the NNO P-phase film splits into three reflections due to the contribution from different twin components (Figure S3c). In general, we conclude that the RSM patterns in our measurements were caused by the orthorhombic unit cells forming a 3-fold symmetric arrangement.

Based on the structural analysis, the phase of the NNO films could be estimated using the out-of-plane lattice *d*-spacing. The N-phase NNO film was stabilized at room temperature rather than at the P phase as the cooling rate increased (Figure 3a). However, with an increase in the gas pressure, the NNO film is stable at the P phase, even with an accelerated rate of cooling of the samples (Figure 3b). Here, a phase diagram for growing the pure NNO N or P phase using PLD is shown in Figure 3c. This phase diagram reveals that the NNO N phase is a metastable phase at room temperature whereas the NNO P phase tends to be stabilized through the formation of twin structures due to its small but non-negligible lattice parameter mismatch with Nb:STO. The P phase is thermodynamically more stable than the N phase at room temperature.

https://doi.org/10.1021/acsami.5c21649
ACS Appl. Mater. Interfaces XXXX, XXX, XXX−XXX

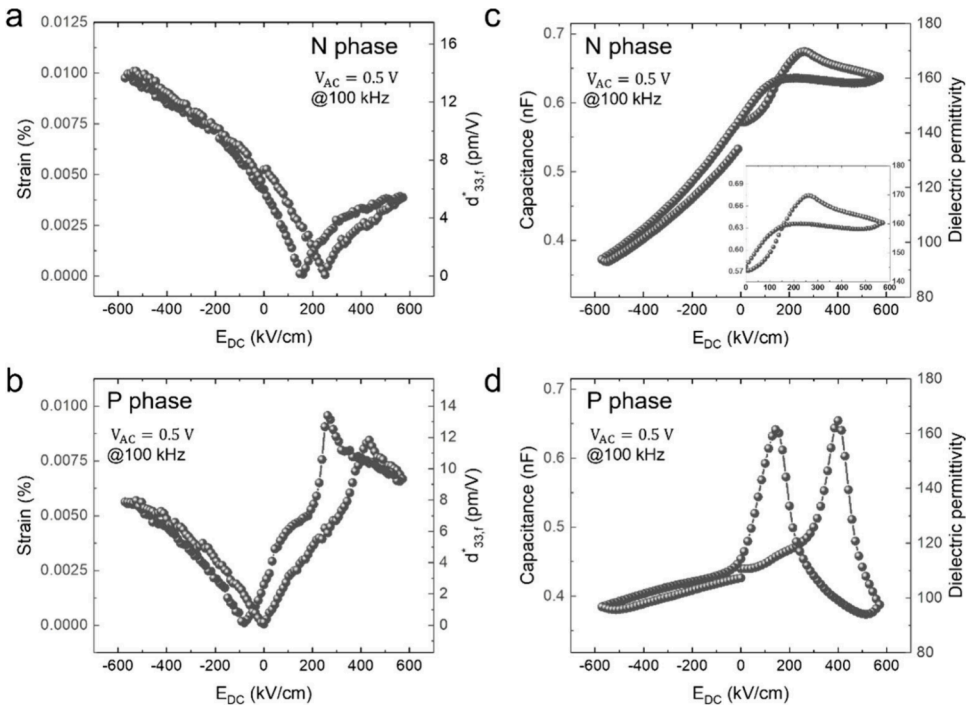

Figure 5. Electromechanical coupling and dielectric characterization of NNO films. Samll signal strain and effective piezoelectric coefficient of (a) N-phase and (b) P-phase NNO films as a function of DC voltage under a 100 kHz, 1 V_{pp} AC drive. Capacitance and dielectric permittivity vs DC voltage of (c) N-phase and (d) P-phase NNO films. The inset of panel c shows a close-up with DC bias from 0 to 600 kV/cm.

Consequently, growth conditions that approach thermodynamic equilibrium favor the formation of the P phase. For example, the NNO film has the P-phase structure at a cooling rate of 5 °C/min, even under low-oxygen pressure conditions. In contrast, when this equilibrium process is broken, such as by excessive atomic kinetic energy during deposition, the formation of twin structures is inhibited, leading to the stabilization of the N phase. A fast cooling rate further helps this kinetic stabilization. Controlling the kinetic energy by tuning the gas pressure has been proven to be an effective method in PVD.[35−37] Consequently, during the preparation process, the introduction of any nonequilibrium factors, such as rapid cooling rates or an increased plasma particle kinetic energy (which can be achieved by reducing the oxygen pressure), can facilitate the formation of the metastable NNO N phase. In addition, previous studies have indicated that variations in the A-site Na content have little influence on the phase structure within a certain compositional range (Na/Nb = 0.9−1.2).[38−40] Our attempts to control the Na and O stoichiometry also confirmed this conclusion (Figure S4), which further supports the idea that the phase-selective growth of NNO is controlled by the kinetic process.

Ferroelectric and Electromechanical Coupling Properties

The natural ferroelectric domains of the N-phase and P-phase NNO films were scanned by using PFM (Figure 4). The surface topography images reveal a smooth surface topography with root-mean-square (RMS) roughness values of ∼950 and ∼230 pm for the N-phase (Figure 4a) and P-phase films (Figure 4d), respectively, consistent with our XRR results, further confirming the good quality of the NNO films. The amplitude and phase images show that the N-phase film has ferroelectric domains with domain sizes of less than 100 nm (Figure 4a). Besides, according to the nature of the *R*3*c* structure and the growth orientation, these ferroelectric domains are 180° domains with the polarization direction up or down. On the contrary, the P-phase NNO thin film has an AFE structure, which reveals the absence of a ferroelectric domain-like amplitude and phase contrast in PFM scanning, as demonstrated in Figure 4d−f. However, when a larger AC drive (2.4 V_{pp}) is applied in the PFM measurement, ferroelectric domain features become discernible in the amplitude and phase images (Figure S5). This phenomenon may originate from the irreversible AFE-to-FE phase transitions triggered by the localized electric field underneath the PFM tip.

The electromechanical coupling and dielectric properties of the NNO films were studied using an integrated LDV and impedance analyzer system, in which the electromechanical strain and capacitance can be measured simultaneously. First, the ferroelectric strain−electric field (*S*−*E*) and capacitance−electric field (*C*−*E*) loop measurements have been implemented to confirm the FE and AFE nature of the NNO films.[41−44] In these electrical characterizations, NNO films were fabricated into 200 μm-diameter Pt/NNO/Nb:STO parallel-plate capacitor devices, and a constant small AC drive (1.0 V_{pp}, 100 kHz) superposed with a varying DC bias was applied to the device; then the surface strain and device capacitance were simultaneously obtained by demodulating the Doppler frequency shift and AC signals (Figure S6).

Figure 5a shows the ferroelectric *S*−*E* loop of the N-phase NNO film, where a butterfly-shaped loop can be observed, indicating the ferroelectricity of this N phase. With an increase in the DC bias, $d^*_{33,f}$ is gradually saturated at ∼14 pm/V, corresponding to a saturated strain of ∼0.01%. Similar results can be obtained from other devices under different AC drive frequencies (Figure S7). Note that the *S*−*E* loop exhibits an obvious shift toward the positive field direction, which is typically attributed to a strong imprint effect in the ferroelectric

https://doi.org/10.1021/acsami.5c21649
ACS Appl. Mater. Interfaces XXXX, XXX, XXX−XXX

film.[45,46] In contrast, the P-phase NNO film shows a significant increase in $d^*_{33,f}$ and strain at a voltage of ~200 kV/cm (Figure 5b), which is attributed to an electric field-driven reconfiguration of antipolar dipoles into a polar ferroelectric state during the AFE-to-FE phase transition. Due to this phase transition, the maximum $d^*_{33,f}$ can be ~14 pm V^{-1} with a strain of ~0.01%. Besides, the P-phase film shows a remnant strain of ~0.003% when the electric field is back to null, confirming the existence of an irreversible AFE-to-FE phase transition. The NNO N phase and P phase both show a hysteresis behavior, suggesting that the domain wall and phase boundary motion also contribute to the strain and $d^*_{33,f}$. Ferroelectric polarization switching results in dielectric permittivity and capacitance peaks or anomalies with respect to the DC bias. Here, the $C-E$ curve of the N-phase film also shows a shifted butterfly shape feature due to the ferroelectric switching with an imprint effect (Figure 5c). However, the double butterfly loop associated with the AFE-to-FE phase transition of the P-phase film retains only the portion corresponding to positive bias (Figure 5d). The phase transition at negative bias may be inhibited due to the Schottky barrier formed at the Pt/NNO interface. This is consistent with our DC $I-V$ testing results, in which the P-phase films show an obvious Schottky rectification behavior (Figure S8).

CONCLUSION

In summary, epitaxial NNO antiferroelectric P-phase and ferroelectric N-phase thin films were successfully grown on (111)-oriented Nb:STO substrates through the precise control of PLD parameters. RSM measurements confirm that the metastable ferroelectric N phase ($R3c$ structure) forms under nonequilibrium growth conditions, while the antiferroelectric P phase ($Pbcm$ structure) is stabilized via a 3-fold twin structure to minimize the interfacial energy with the Nb:STO substrate. PFM measurements demonstrate that the N phase exhibits nanoscale ferroelectric domains, whereas the P phase shows field-induced AFE-to-FE transitions, leading to enhanced piezoelectric coefficients. This work demonstrated that the NNO-phase composition is strongly correlated with the crystal structure, ferroelectric properties, and electromechanical responses, providing a path for tailoring NNO thin films toward functional device applications.

EXPERIMENTAL SECTION

Thin Film Preparation

NNO ceramic targets for PLD growth were synthesized via conventional solid-state reaction methods using Na_2CO_3 (99.0%) and Nb_2O_5 (99.9%) powders as the raw materials. NNO films with a thickness of 70 nm were epitaxially grown on single-crystal Nb:STO (111) substrates (Hefei Kejing, China) by ablating the NNO ceramic target with a 248 nm KrF excimer laser (COMPex 205, Coherent). Nb:STO substrates were sequentially cleaned in acetone, ethanol, and deionized water for 5 min each prior to PLD growth. NNO thin films were grown at 800 °C under oxygen partial pressures of 22 and 54 Pa. The laser energy density was maintained at approximately 2 J/cm^2 with a repetition rate of 10 Hz. Film deposition was always performed in an on-axis geometry with a target−substrate distance of 6.5 cm. After film deposition, the samples were cooled to room temperature at varying cooling rates (5, 7.5, and 10 °C/min) under an oxygen partial pressure of 10 kPa.

Characterization

NNO crystal structure models in panels a and b of Figure 1 were generated by using VESTA 3.[47] High-resolution X-ray diffraction (XRD) and low-angle X-ray reflectivity (XRR) (SmartLab, Rigaku) with Cu Kα radiation (λ = 1.5405 Å) were used to characterize the crystal structure. The lattice parameters of the NNO P phase were calculated based on the reciprocal space vector (RSV) method.[34] Half-order and quarter-order reflection measurements were conducted at the XDD beamline of the Singapore Synchrotron Light Source using X-rays with a wavelength of 1.5400 Å. Ferroelectric domains were imaged in the PFM mode using a Pt-coated conductive probe (240AC-PP, OPUS). Circular Pt top electrodes with a diameter of 200 μm and a thickness of 100 nm were fabricated by UV lithography and e-beam evaporation deposition. An integrated LDV (OFV-5000, Polytec) and impedance analyzer (MFIA, Zurich Instruments) system has been utilized to simultaneously measure the surface vibration amplitude and capacitance of the Pt/NNO/Nb:STO devices under varying DC biases. DC $I-V$ measurements were performed by using a sourcemeter (Keithley 2450, Tektronix).

ASSOCIATED CONTENT

Supporting Information

The Supporting Information is available free of charge at https://pubs.acs.org/doi/10.1021/acsami.5c21649.

Additional data, including XRR, XRD, PFM, $S-E$ loop, $I-V$ curve, and crystal structure parameter data and schematics (PDF)

AUTHOR INFORMATION

Corresponding Authors

Huajun Liu − *Institute of Materials Research and Engineering (IMRE), Agency for Science, Technology and Research (A*STAR), Singapore 138634, Republic of Singapore; School of Materials Science and Engineering, Nanyang Technological University, Singapore 639798, Republic of Singapore;* orcid.org/0000-0002-0540-6486; Email: liu_huajun@a-star.edu.sg

Yeng Ming Lam − *School of Materials Science and Engineering, Nanyang Technological University, Singapore 639798, Republic of Singapore; Facility for Analysis, Characterisation, Testing and Simulation (FACTS), Nanyang Technological University, Singapore 639798, Republic of Singapore;* orcid.org/0000-0001-9390-8074; Email: ymlam@ntu.edu.sg

Authors

Baichen Lin − *Institute of Materials Research and Engineering (IMRE), Agency for Science, Technology and Research (A*STAR), Singapore 138634, Republic of Singapore; School of Materials Science and Engineering, Nanyang Technological University, Singapore 639798, Republic of Singapore*

Qibin Zeng − *Institute of Materials Research and Engineering (IMRE), Agency for Science, Technology and Research (A*STAR), Singapore 138634, Republic of Singapore*

Ping Yang − *Singapore Synchrotron Light Source (SSLS), National University of Singapore, Singapore 117603, Republic of Singapore*

Shengwei Zeng − *Institute of Materials Research and Engineering (IMRE), Agency for Science, Technology and Research (A*STAR), Singapore 138634, Republic of Singapore*

Zhi Shiuh Lim − *Institute of Materials Research and Engineering (IMRE), Agency for Science, Technology and Research (A*STAR), Singapore 138634, Republic of Singapore*

https://doi.org/10.1021/acsami.5c21649
ACS Appl. Mater. Interfaces XXXX, XXX, XXX−XXX

Tiancheng Luo − *Institute of Materials Research and Engineering (IMRE), Agency for Science, Technology and Research (A*STAR), Singapore 138634, Republic of Singapore*
Weifan Cai − *Institute of Materials Research and Engineering (IMRE), Agency for Science, Technology and Research (A*STAR), Singapore 138634, Republic of Singapore*
Samantha Faye Duran Solco − *Institute of Materials Research and Engineering (IMRE), Agency for Science, Technology and Research (A*STAR), Singapore 138634, Republic of Singapore*
Zhen Ye − *Institute of Materials Research and Engineering (IMRE), Agency for Science, Technology and Research (A*STAR), Singapore 138634, Republic of Singapore; Department of Mechanical Engineering, National University of Singapore, Singapore 117575, Republic of Singapore*
Celine Sim − *Institute of Materials Research and Engineering (IMRE), Agency for Science, Technology and Research (A*STAR), Singapore 138634, Republic of Singapore; School of Materials Science and Engineering, Nanyang Technological University, Singapore 639798, Republic of Singapore;* orcid.org/0000-0003-4316-1974
Jinlong Xu − *Institute of Materials Research and Engineering (IMRE), Agency for Science, Technology and Research (A*STAR), Singapore 138634, Republic of Singapore; Department of Electrical and Computer Engineering, National University of Singapore, Singapore 117583, Republic of Singapore*
Mengyao Xiao − *Institute of Materials Research and Engineering (IMRE), Agency for Science, Technology and Research (A*STAR), Singapore 138634, Republic of Singapore; Department of Electrical and Computer Engineering, National University of Singapore, Singapore 117583, Republic of Singapore*
Khuong Phuong Ong − *Institute of High Performance Computing (IHPC), A*STAR (Agency for Science, Technology and Research), Singapore 138632, Republic of Singapore*
Chee Kiang Ivan Tan − *Institute of Materials Research and Engineering (IMRE), Agency for Science, Technology and Research (A*STAR), Singapore 138634, Republic of Singapore*
Seeram Ramakrishna − *Department of Mechanical Engineering, National University of Singapore, Singapore 117575, Republic of Singapore*
Mark B. H. Breese − *Singapore Synchrotron Light Source (SSLS), National University of Singapore, Singapore 117603, Republic of Singapore*
Chengkuo Lee − *Department of Electrical and Computer Engineering, National University of Singapore, Singapore 117583, Republic of Singapore;* orcid.org/0000-0002-8886-3649
Kaiyang Zeng − *Department of Mechanical Engineering, National University of Singapore, Singapore 117575, Republic of Singapore;* orcid.org/0000-0002-3348-0018

Complete contact information is available at: https://pubs.acs.org/10.1021/acsami.5c21649

Notes

The authors declare no competing financial interest.

ACKNOWLEDGMENTS

B.L. acknowledges the support of the Singapore International Graduate Award (SINGA), A*STAR. The authors acknowledge funding support by the National Research Foundation Competitive Research Program (NRF-CRP28-2022-0002), a RIE2025 MTC Individual Research Grant (M22K2c0084), the Career Development Fund (C210812020), and the Central Research Fund, A*STAR, Singapore.

REFERENCES

(1) Dawber, M.; Rabe, K. M.; Scott, J. F. Physics of thin-film ferroelectric oxides. *Rev. Mod. Phys.* **2005**, *77* (4), 1083−1130.
(2) Fernandez, A.; Acharya, M.; Lee, H. G.; Schimpf, J.; Jiang, Y.; Lou, D.; Tian, Z.; Martin, L. W. Thin-Film Ferroelectrics. *Adv. Mater.* **2022**, *34* (30), No. e2108841.
(3) Liu, C.; Si, Y.; Zhang, H.; Wu, C.; Deng, S.; Dong, Y.; Li, Y.; Zhuo, M.; Fan, N.; Xu, B.; Lu, P.; Zhang, L.; Lin, X.; Liu, X.; Yang, J.; Luo, Z.; Das, S.; Bellaiche, L.; Chen, Y.; Chen, Z. Low voltage-driven high-performance thermal switching in antiferroelectric $PbZrO_3$ thin films. *Science* **2023**, *382* (6676), 1265−1269.
(4) Si, Y.; Fan, N.; Dong, Y.; Ye, Z.; Deng, S.; Li, Y.; Zhou, C.; Zeng, Q.; You, L.; Zhu, Y.; Luo, Z.; Das, S.; Bellaiche, L.; Xu, B.; Liu, H.; Chen, Z. Ideal antiferroelectricity with large digital electrostrain in $PbZrO_3$ epitaxial thin films. *Nat. Commun.* **2025**, *16* (1), 4263.
(5) Pan, H.; Zhu, M.; Banyas, E.; Alaerts, L.; Acharya, M.; Zhang, H.; Kim, J.; Chen, X.; Huang, X.; Xu, M.; Harris, I.; Tian, Z.; Ricci, F.; Hanrahan, B.; Spanier, J. E.; Hautier, G.; LeBeau, J. M.; Neaton, J. B.; Martin, L. W. Clamping enables enhanced electromechanical responses in antiferroelectric thin films. *Nat. Mater.* **2024**, *23* (7), 944−950.
(6) Zhang, M. H.; Ding, H.; Egert, S.; Zhao, C.; Villa, L.; Fulanovic, L.; Groszewicz, P. B.; Buntkowsky, G.; Kleebe, H. J.; Albe, K.; Klein, A.; Koruza, J. Tailoring high-energy storage $NaNbO_3$-based materials from antiferroelectric to relaxor states. *Nat. Commun.* **2023**, *14* (1), 1525.
(7) Liu, H.; Wu, H.; Ong, K.-P.; Yang, T.; Yang, P.; Das, P. K.; Chi, X.; Zhang, Y.; Diao, C.; Wong, W. K. A.; Chew, E. P.; Chen, Y. F.; Tan, C. K. I.; Rusydi, A.; Breese, M. B. H.; Singh, D. J.; Chen, L.-Q.; Pennycook, S. J.; Yao, K. Giant piezoelectricity in oxide thin films with nanopillar structure. *Science* **2020**, *369*, 292−297.
(8) Lin, B.; Ong, K. P.; Yang, T.; Zeng, Q.; Hui, H. K.; Ye, Z.; Sim, C.; Yen, Z.; Yang, P.; Dou, Y.; Li, X.; Gao, X.; Tan, C. K. I.; Lim, Z. S.; Zeng, S.; Luo, T.; Xu, J.; Tong, X.; Li, P. W. F.; Ren, M.; Zeng, K.; Sun, C.; Ramakrishna, S.; Breese, M. B. H.; Boothroyd, C.; Lee, C.; Singh, D. J.; Lam, Y. M.; Liu, H. Ultrahigh electromechanical response from competing ferroic orders. *Nature* **2024**, *633* (8031), 798−803.
(9) Mishra, S. K.; Choudhury, N.; Chaplot, S. L.; Krishna, P. S. R.; Mittal, R. Competing antiferroelectric and ferroelectric interactions in $NaNbO_3$: Neutron diffraction and theoretical studies. *Phys. Rev. B* **2007**, *76* (2), 024110.
(10) Megaw, H. D. The seven phases of sodium niobate. *Ferroelectrics* **1974**, *7* (1), 87−89.
(11) Darlington, C. N. W.; Megaw, H. D. The low-temperature phase transition of sodium niohate and the structure of the low-temperature phase, N. *Acta Crystallogr.* **1973**, *B29*, 2171.
(12) Mishchuk, D. O.; V'yunov, O. I.; Ovchar, O. V.; Belous, A. G. Structural and dielectric properties of solid solutions of sodium niobate in lanthanum and neodymium niobates. *Inorg. Mater.* **2004**, *40* (12), 1324−1330.
(13) Schneider, T.; Cardoletti, J.; Ding, H.; Zhang, M.-H.; Jiang, T.; Major, M.; Komissinskiy, P.; Molina-Luna, L.; Alff, L. Evidence for antipolar displacements in $NaNbO_3$ thin films. *Appl. Phys. Lett.* **2022**, *121* (12), 122906.
(14) Zhang, M.-H.; Fulanović, L.; Egert, S.; Ding, H.; Groszewicz, P. B.; Kleebe, H.-J.; Molina-Luna, L.; Koruza, J. Electric-field-induced antiferroelectric to ferroelectric phase transition in polycrystalline $NaNbO_3$. *Acta Mater.* **2020**, *200*, 127−135.

(15) Zhang, M.-H.; Hadaeghi, N.; Egert, S.; Ding, H.; Zhang, H.; Groszewicz, P. B.; Buntkowsky, G.; Klein, A.; Koruza, J. Design of lead-free antiferroelectric (1 - x)$NaNbO_3$-x$SrSnO_3$ compositions guided by first-principles calculations. *Chem. Mater.* **2021**, *33* (1), 266−274.
(16) Zhang, M.-H.; Fulanović, L.; Zhao, C.; Koruza, J. Review on field-induced phase transitions in lead-free $NaNbO_3$-based antiferroelectric perovskite oxides for energy storage. *J. Materiomics* **2023**, *9* (1), 1−18.
(17) Machado, R.; Sepliarsky, M.; Stachiotti, M. G. Relative phase stability and lattice dynamics of $NaNbO_3$ from first-principles calculations. *Phys. Rev. B* **2011**, *84* (13), 134107.
(18) Sakowski-Cowley, A. C.; Łukaszewicz, K.; Megaw, H. D. The structure of sodium niobate at room temperature, and the problem of reliability in pseudosymmetric structures. *Acta Crystallogr.* **1969**, *B25* (5), 851−865.
(19) Trolier-Mckinstry, S.; Muralt, P. Thin film piezoelectrics for MEMS. *J. Electroceramics* **2004**, *12*, 7−17.
(20) Katsumata, K.; Cordonier, C. E.; Shichi, T.; Fujishima, A. Photocatalytic activity of $NaNbO_3$ thin films. *J. Am. Chem. Soc.* **2009**, *131* (11), 3856−3857.
(21) Saito, T.; Adachi, H.; Wada, T.; Adachi, H. Pulsed-Laser Deposition of Ferroelectric $NaNbO_3$ Thin Films. *Jpn. J. Appl. Phys.* **2005**, *44* (9S), 6969.
(22) Sellmann, J.; Schwarzkopf, J.; Kwasniewski, A.; Schmidbauer, M.; Braun, D.; Duk, A. Strained ferroelectric $NaNbO_3$ thin films: Impact of pulsed laser deposition growth conditions on structural properties. *Thin Solid Films* **2014**, *570*, 107−113.
(23) Schneider, T.; Cardoletti, J.; Komissinskiy, P.; Alff, L. Impact of Strain Engineering on Antiferroelectricity in $NaNbO_3$ Thin Films. *ACS Omega* **2023**, *8* (26), 23587−23595.
(24) Zeng, S.; Ong, K. P.; Solco, S. F. D.; Lim, Z. S.; Zeng, Q.; Lin, B.; Luo, J.; Zhao, W.; Luo, T.; Cai, W.; Ye, Z.; Sim, C.; Tan, C. K. I.; Ramakrishna, S.; Lam, Y. M.; Ariando, A.; Liu, H. Identifying the Limits of Strain Engineering in $NaNbO_3$ Ultrathin Films. *ACS Appl. Mater. Interfaces* **2025**, *17* (30), 43227−43234.
(25) Schmidbauer, M.; Sellmann, J.; Braun, D.; Kwasniewski, A.; Duk, A.; Schwarzkopf, J. Ferroelectric domain structure of $NaNbO_3$ epitaxial thin films grown on (110) $DyScO_3$ substrates. *pss RRL* **2014**, *8* (6), 522−526.
(26) Nakagawara, O.; Shimuta, T.; Makino, T.; Arai, S.; Tabata, H.; Kawai, T. Epitaxial growth and dielectric properties of (111) oriented $BaTiO_3$/$SrTiO_3$ superlattices by pulsed-laser deposition. *Appl. Phys. Lett.* **2000**, *77* (20), 3257−3259.
(27) Wördenweber, R.; Schwarzkopf, J.; Hollmann, E.; Duk, A.; Cai, B.; Schmidbauer, M. Impact of compressive in-plane strain on the ferroelectric properties of epitaxial $NaNbO_3$ films on (110) $NdGaO_3$. *Appl. Phys. Lett.* **2013**, *103* (13), 132908.
(28) He, J.; Borisevich, A.; Kalinin, S. V.; Pennycook, S. J.; Pantelides, S. T. Control of octahedral tilts and magnetic properties of perovskite oxide heterostructures by substrate symmetry. *Phys. Rev. Lett.* **2010**, *105* (22), 227203.
(29) Jin, W. T.; Gretarsson, H.; Jang, S. Y.; Kim, C.-Y.; Noh, T. W.; Kim, Y.-J. Hidden structural transition in epitaxial $Ca_{0.5}Sr_{0.5}IrO_3$/$SrTiO_3$ thin film. *Phys. Rev. Mater.* **2019**, *3* (10), 103604.
(30) Wang, D. Y.; Chan, N. Y.; Zheng, R. K.; Kong, C.; Lin, D. M.; Dai, J. Y.; Chan, H. L. W.; Li, S. Multiferroism in orientational engineered (La, Mn) co-substituted $BiFeO_3$ thin films. *J. Appl. Phys.* **2011**, *109* (11), 114105.
(31) Yamazoe, S.; Kohori, A.; Sakurai, H.; Kitanaka, Y.; Noguchi, Y.; Miyayama, M.; Wada, T. Laser beam scanning microscope and piezoresponse force microscope studies on domain structured in 001-, 110-, and 111-oriented $NaNbO_3$ films. *J. Appl. Phys.* **2012**, *112* (5), 052007.
(32) Liu, H.; Yang, P.; Yao, K.; Wang, J. Twinning rotation and ferroelectric behavior of epitaxial $BiFeO_3$ (001) thin film. *Appl. Phys. Lett.* **2010**, *96* (1), 012901.
(33) Chen, Z.; Luo, Z.; Huang, C.; Qi, Y.; Yang, P.; You, L.; Hu, C.; Wu, T.; Wang, J.; Gao, C.; Sritharan, T.; Chen, L. Low-Symmetry Monoclinic Phases and Polarization Rotation Path Mediated by Epitaxial Strain in Multiferroic $BiFeO_3$ Thin Films. *Adv. Funct. Mater.* **2011**, *21* (1), 133−138.
(34) Yang, P.; Liu, H.; Chen, Z.; Chen, L.; Wang, J. Unit-cell determination of epitaxial thin films based on reciprocal-space vectors by high-resolution X-ray diffractometry. *J. Appl. Crystallogr.* **2014**, *47* (1), 402−413.
(35) Kotsonis, G. N.; Rost, C. M.; Harris, D. T.; Maria, J.-P. Epitaxial entropy-stabilized oxides: growth of chemically diverse phases via kinetic bombardment. *MRS Commun.* **2018**, *8* (3), 1371−1377.
(36) Wohlgemuth, M. A.; Trstenjak, U.; Sarantopoulos, A.; Gunkel, F.; Dittmann, R. Control of growth kinetics during remote epitaxy of complex oxides on graphene by pulsed laser deposition. *APL Mater.* **2024**, *12* (2), 021113.
(37) Warrender, J. M.; Aziz, M. J. Kinetic energy effects on morphology evolution during pulsed laser deposition of metal-on-insulator films. *Phys. Rev. B* **2007**, *75* (8), ZZZ DOI: 10.1103/PhysRevB.75.085433.
(38) Dong, H.; Luo, B.; Jin, K. Tunable dielectric and energy storage properties in nonstoichiometric $NaNbO_3$ thin films. *Ceram. Int.* **2022**, *48* (11), 16215−16220.
(39) Hussain, A.; Gadelmawla, A.; Maier, J. G.; Eyoum, G. E.; Miyazaki, H.; Kimura, K.; Hayashi, K.; Webber, K. G. Effect of A-site non-stoichiometry in $NaNbO_3$ ceramics. *Scr. Mater.* **2025**, *255*, 116384.
(40) Fan, Y.; Zhou, Z.; Liang, R.; Zhou, M.; Dong, X. The effect of A-site nonstoichiometry on the microstructure, electric properties, and phase stability of $NaNbO_3$ polycrystalline ceramics. *J. Eur. Ceram. Soc.* **2019**, *39* (15), 4712−4718.
(41) Boni, A. G.; Chirila, C. F.; Negrea, R.; Ghica, C.; Pasuk, I.; Pintilie, I.; Pintilie, L. Electrical Properties of Epitaxial Ferroelectric Heterostructures. In *Epitaxy*; InTech, 2018.
(42) Koval, V.; Viola, G.; Tan, Y. Biasing Effects in Ferroic Materials. In *Ferroelectric Materials - Synthesis and Characterization*; InTech, 2015.
(43) Lu, H.; Glinsek, S.; Buragohain, P.; Defay, E.; Iñiguez, J.; Gruverman, A. Probing Antiferroelectric-Ferroelectric Phase Transitions in $PbZrO_3$ Capacitors by Piezoresponse Force Microscopy. *Adv. Funct. Mater.* **2020**, *30* (45), 2003622.
(44) Yao, Y.; Naden, A.; Tian, M.; Lisenkov, S.; Beller, Z.; Kumar, A.; Kacher, J.; Ponomareva, I.; Bassiri-Gharb, N. Ferrielectricity in the archetypal antiferroelectric, $PbZrO_3$. *Adv. Mater.* **2023**, *35* (3), No. e2206541.
(45) Kadota, Y.; Hosaka, H.; Morita, T. Shape Memory Piezoelectric Actuator by Control of the Imprint Electrical Field. *Ferroelectrics* **2008**, *368* (1), 185−193.
(46) Lee, H.; Kim, T. H.; Patzner, J. J.; Lu, H.; Lee, J. W.; Zhou, H.; Chang, W.; Mahanthappa, M. K.; Tsymbal, E. Y.; Gruverman, A.; Eom, C. B. Imprint Control of $BaTiO_3$ Thin Films via Chemically Induced Surface Polarization Pinning. *Nano Lett.* **2016**, *16* (4), 2400−2406.
(47) Momma, K.; Izumi, F. VESTA 3 for three-dimensional visualization of crystal, volumetric and morphology data. *J. Appl. Crystallogr.* **2011**, *44* (6), 1272−1276.

https://doi.org/10.1021/acsami.5c21649
ACS Appl. Mater. Interfaces XXXX, XXX, XXX−XXX